Investigations of Droplet-Plasma Interaction using Multi-dimensional Coupled Model

M. M. Iqbal[1*] and **M. M. Turner**[1]

Key words Multi-dimensional modelling, Droplet-plasma interaction, Two phase flow, Atmospheric pressure plasma.

Recently developed multi-dimensional coupled fluid-droplet model is used to investigate the behavior of complex interaction between the liquid precursor droplets and atmospheric pressure plasma (APP). The significance of this droplet-plasma interaction is not well understood under diverse realm of working conditions in two-phase flow. In this study, we explain the implication of vaporization of liquid droplets in APP which are subsequently responsible to control major characteristics of surface coating depositions. Coalescence of water droplets is more dominant than Hexamethyldisiloxane (HMDSO) droplets because of its sluggish rate of evaporation. A disparity in the performance of evaporation is identified in two independent mediums, such as gas mixture and discharge plasma using HMDSO precursor. The length evaporation of droplets is amplified by an increment of gas flow rate indicating with a reduction in the gas temperature and electron mean energy. In particular, the spatio-temporal density distributions of charged particles show a clear pattern in which the typical nitrogen impurity ions are primarily effective as compared to other helium ionic species along the pulse of droplets in APP. Finally, we contrast the behavior of discharge species in the pure helium and He-N_2 gas mixtures revealing the importance of stepwise and Penning ionization processes.

Copyright line will be provided by the publisher

School of Physical Sciences and National Centre for Plasma Science and Technology, Dublin City University, Glasnevin, Dublin 9, Ireland.[1]

1 Introduction

The direct introduction of liquid precursors into atmospheric pressure plasma has been considered as practically useful for many applications, ranging from the industrial plasma processes to medical treatments, such as plasma-enhanced chemical vapour deposition [1], sterilization of medical equipments [2], tissue engineering and direct treatment of skin diseases [3, 4]. The operation of droplet deformation, solidification and heat transfer mechanisms in the substrate have been explained by solving the Navier-Stokes and energy equations in [5]. For plasma surface deposition, which is an immediate motivation for the present work, it may be desirable for droplets to evaporate entirely in the plasma, and most undesirable for partially evaporated droplets to reach on the substrate surface [6]. The functional characteristics of surface deposition depend on numerous factors, such as precursor and gas flow rates and in particular, the composition of the gas mixture that is mainly responsible to customize the operation of deposition coating because of involving various chemical interactions during the evaporation of droplets and particulate nucleation [7]. Penning ionization has been considered as an exciting activity in the presence of trace amount of nitrogen impurities in the helium gas mixture [8]. In the last two decades, there have been serious efforts to control the desired aspects of APP during processing in many branches of industry, which produced several satisfactory outcomes using low frequency RF plasma sources ranging from 0.1 kHz to 100 kHz [$9-12$].

Intricate interaction of gas with liquid precursors was explained for the operation of spray dryers, which mainly included evaporation of droplets as well as mutual interactions between them in the case of small Weber numbers [13]. It has been observed in the experiments that the uniform deposition of coating on silicon substrate surfaces can be obtained by the adjustment of flow rates of liquid precursors in the PlasmaStream^{TM} atmospheric pressure plasma jet deposition system [14]. The influential activities, such as desolvation, breakup and coalescence of droplets were performed an important role to alter the features of an inductively coupled plasma as demonstrated in [15]. The precise procedure for simulating two-phase flow is based on the approach of Eulerian-Lagrangian

[1] Corresponding author: e-mail:iqbalm3@mail.dcu.ie, Phone: +00 353 1 700 7787, Fax: +353 1 700 8484

Copyright line will be provided by the publisher

method to explore the crucial attributes of interaction between the liquid droplets and flowing gas [16, 17, 18] in different applications of combustion, which have been verified by the spectroscopic observations in [19] containing signal fluctuations. In experiments, the efficiency of spectroscopic results can be improved by dissolving an entire bundle of liquid droplets into discharge plasma as compared to fragmentary vaporization of droplets [20]. The overall dynamics of droplets are updated by the domination of several forces, such as electrical, aerodynamic, surface tension, internal viscous and gravity during downward fall in discharge plasmas [21].

In this paper, we have discussed the significance of droplet-plasma interaction during the transport of liquid precursor droplets in the plasma chamber. The purpose of this simulation study is to provide the operating conditions under which homogeneous uniform deposition can be obtained on the substrate surface. For this, we employed a two-dimensional coupled fluid-droplet model to express the interaction in two-phase flow that incorporates the progress of evaporation as well as collision mechanisms, such as grazing and coalescence between liquid droplets. The characteristics of APP are modified by the variation of gas flow rates, which show that the gas temperature and the mean energy of electrons along the pulse of droplets are reduced by an increment of gas flow rates. Specifically, we discuss the primary contribution of Penning ionization during the droplet-plasma interaction in the proximity of droplets in the pure helium and He-N_2 gas mixtures. The consequences of distinct precursors are analyzed in APP indicating the superiority of evaporation than other mutual interactions between the droplets. Finally, the iso-contours in three-dimensional space are elucidated to explore the interaction in two-phase flow using Tetraethyl orthosilicate (TEOS) and HMDSO precursors in the atmospheric pressure plasma at three distinct time instants.

2 Two-dimensional Coupled Fluid-Droplet Model

In coupled 2D fluid-droplet model, the interaction between liquid droplets and discharge plasma refers to the exchange of aspects between two-phase flow. The liquid phase is handled by Lagrangian method using X-squared distribution of precursor droplets, while the Eulerian approach is applied to describe the operating gas mixture including all chemical reactions mentioned in [22]. The models for the liquid droplets and gas mixture are joined together through the coupling source terms that add to the fluid model equations of mass density, momentum and energy of atmospheric pressure plasma and the liquid droplets. The following set of equations is employed for the modelling of plasma fluid as

$$\frac{\partial \rho_{gas}}{\partial t_1} + \rho_{gas} a \overrightarrow{\nabla} . \overrightarrow{u}(r,z,t) = S \tag{1}$$

$$\frac{\partial \left(\rho_{gas} \overrightarrow{u}(r,z,t)\right)}{\partial t_1} = \overrightarrow{\nabla} P + \overrightarrow{\nabla} . \overrightarrow{\Gamma}_{\mu} \nabla \overrightarrow{u}(r,z,t) + S_M \tag{2}$$

$$\frac{\partial \left(\rho_{gas} h_{gas}\right)}{\partial t_1} = \overrightarrow{\nabla} . \frac{k}{C_p} \nabla h + \overrightarrow{j} . \overrightarrow{E} + S_E \tag{3}$$

$$\frac{\partial \left(Y \rho_{gas}\right)}{\partial t_1} = \overrightarrow{\nabla} . D_{AB} \nabla Y + S \tag{4}$$

Where the symbols along with their details mentioned in the set of Eqs. $(1-4)$ are specified in Table 1. The Implicit Continuous Eulerian (ICE) approach [13, 16] is applied to characterize the behavior of the gas flow in which the momentum transfer takes place between two-phase flow in the plasma chamber. We consider major discharge species, such as electrons (e^-), atomic helium (He^+) ions, molecular helium and nitrogen (He_2^+, N_2^+) ions and metastables (He^*) for the numerical modelling of the atmospheric pressure plasma in two-phase flow. The continuity equation is numerically solved for the mentioned discharge plasma species, which is expressed as

$$\frac{\partial n_{sp}(r,z,t)}{\partial t_2} + \overrightarrow{\nabla} . \left(\overrightarrow{\Phi}_{sp}(r,z,t) + n_{sp} \overrightarrow{u}(r,z,t) \right) = S_{sp} \tag{5}$$

Here n_{sp}, $\overrightarrow{\Phi}_{sp}(r,z,t) = |q_{sp}| \, \mu_{sp} \overrightarrow{E} n_{sp} - D_{sp} \overrightarrow{\nabla} n_{sp}$ and S_{sp} correspond to the plasma species density, drift-diffusion flux and source terms for the generation and destruction of plasma species for the entire set of chemical reactions as mentioned in [22]. The electric field is evaluated by employing Poisson's equation, which is used

Copyright line will be provided by the publisher

in the fluid equations of atmospheric pressure plasma considering the asymmetric electrode geometry of the PlasmaStream system as described in [23]. In order to evaluate the electric field ($\overrightarrow{E}$), the Poisson's equation can be expressed as

$$\overrightarrow{\nabla}.\left(\epsilon_0 \overrightarrow{E}(r,z,t)\right) = -\sum_s q_{sp} n_{sp}(r,z,t) \tag{6}$$

Where $q_{sp}n_{sp}$ corresponds to the space charge density and ϵ_0 is the permittivity of the free space. Thus the strengths of electric field in two-dimensional space are calculated from the gradient of the electric potential along r and z directions as $E_r = -\partial V/\,\partial r$ and $E_z = -\partial V/\,\partial z$, where $V = V_0 \sin(2\pi f t)$ is an oscillating sinusoidal potential imposed on the thin metal electrode and the substrate is grounded. The dynamic position of liquid droplets is traced by estimating their position, velocity, radius and temperature of droplets during downward drag in the plasma chamber as

$$\frac{d\overrightarrow{x}_p}{dt_1} = \overrightarrow{u}_p \tag{7}$$

$$\frac{d\overrightarrow{u}_p}{dt_1} = K_p(\overrightarrow{u} + \overrightarrow{u}' - \overrightarrow{u}_d) - (1/\rho_l)\overrightarrow{\nabla} p + g_z \widehat{k} + |q_p|\,\overrightarrow{E}/m_p \tag{8}$$

$$\frac{dr_p}{dt_1} = \left(\frac{\lambda_{gas}}{\rho_l c_{p_{gas}}}\right)\left(\frac{Nu_{gas}}{2r_p}\right)\left(\frac{Y_{V_s} - Y_V}{1 - Y_{V_s}}\right) \tag{9}$$

$$\frac{dT_p}{dt_1} = \left(\left(\frac{3\lambda_l N u_l}{2\rho_l c_l r_p^2}\right) + 3\frac{\left(\frac{dr_p}{dt_1}\right)}{r_p}\right)(T_s - T_p) \tag{10}$$

Regarding the charging of droplets in atmospheric pressure plasma, we assume that the flux of electrons is balanced with ions on the surface of the droplets and hence the net current becomes zero. The charge on the surface of the droplet is obtained by using the following formula ($q_d = 4\pi\epsilon_0 r_d \Delta\, V_f$), where the floating potential ($\Delta\, V_f$) [24, 25] on the surface of the droplet is evaluated as

$$\Delta\, V_f = \frac{k_B T_e}{q_e} \log\left(\frac{4 n_i v_i}{n_e \overline{v}_e}\right) \tag{11}$$

where the description of symbols used in the above set of Eqs. $(1-11)$ are mentioned in Table 1.

2.1 Initial and boundary conditions

In multi-dimensional coupled fluid-droplet model, we have used the similar boundary conditions as discussed in [23]; however, the input operating parameters are highlighted in Table 2. In the plasma chamber, the gas flow is introduced at two distinct positions of inlet with gas flow rates (Q_1 and Q_2 μL min^{-1}) respectively, whereas the laminar profiles of velocity are assumed at the entrance boundary. At the outlet plane, the axial gradients are supposed as zero. The nebulizer droplets are injected from the pivotal position using a pneumatic nebulizer with a flow rate of Q_3 μL min^{-1} while interacting directly with plasma stream, but the peculiarity of two-phase is updated if the point of injection of droplets is modified. Initially, the value of gas temperature is assumed as room temperature (300 K) in the atmospheric pressure plasma. The numerical method of solving these equations as well as the entire set of particulars dealing with the geometry of plasma reactor are described earlier in the above mentioned reference. The initial injection velocity of droplets is not similar in different sections of this paper.

Copyright line will be provided by the publisher

Table 2: Initial values employed in the fluid-droplet model

Variables used in Fluid-Droplet Model (FD2d)	**Initial Input Values**
Initial density of discharge species at $t = 0.0$	$\sim 1.0 \times 10^9$ cm^{-3}
frequency (f)	20 kHz
Magnitude of applied voltage (V_0)	13.5 kV
Operating pressure (P)	760.0 Torr
Amount of nitrogen impurities in Helium gas	50 ppm
Gas temperature (T_g) at $t = 0.0$	300 K
Initial temperature (T_d) of liquid droplets	295 K
Components of droplet velocities (u_r, u_z)	$(0.001, 1500)$ cm sec^{-1}
Mass density of gas (ρ_{gas})	0.1617×10^{-3} g cm^{-3}
Initial vapour species mass fraction (Y)	1.00×10^{-2}
Helium gas diffusivity	1.6313 cm^2 sec^{-1}
Time step (Δt_1) for droplets and gas phases	0.10×10^{-5} sec
Plasma time step (Δt_2)	1.00×10^{-9} sec
Electron mean energy at $t = 0.0$	0.5 eV
Mean energy of ions at $t = 0.0$	0.026 eV

3 Results and Discussion

We have elaborated the outcomes of two-dimensional coupled fluid-droplet model in two major parts. In the first part, the behavior of the pulse of water droplets is demonstrated by providing a precise description of the droplet counts and size distributions as well as their surging effects in the neutral gas mixture. The significance of evaporation of droplets is analyzed in two different mediums, such as He-N_2 gas mixture and APP under similar accomplishing conditions to explore the effectiveness of atmospheric pressure plasma. The consequences of mutual interactions between the droplets during downward flight are crucial in the case of water droplets as compared to the HMDSO droplets. In fact, the length of the evaporation channel in the discharge plasma is escalated with an increment of the central gas flow rate. In the second part, the response of different liquid precursors, such as HMDSO, nHexane, TEOS and water in APP is contrasted to describe the divergence of evaporation of droplets using similar initial constraints. It is recognized from the production rates of metastables that they responsible to maintain the sufficient level of ionization around the pulse of droplets through stepwise ionization mechanism in the pure helium, while Penning ionization replaces its place in He-N_2 gas mixture. In addition, the three-dimensional elucidation of droplets' evaporation provides a clear indication that its spread gradually expands during the downward fall of droplets in the plasma chamber.

3.1 Evaporation of water droplets in APP

Initially, a pulse of water droplets is injected into the PlasmaStream system through the nebulizer, which interacts with helium atmospheric pressure plasma containing trace amount of nitrogen impurities. These liquid droplets perturb the uniform atmospheric pressure plasma and then acquiring a charge on the surface of droplet due to the greater thermal flux of electrons than ions. A sheath forms around the surface of water droplet in APP as explained in [26]. During this interaction, several forces are acting on the droplets simultaneously, such as electrical ($|q_d| \overrightarrow{E}$), aerodynamic drag ($K_p(\overrightarrow{u} + \overrightarrow{u}' - \overrightarrow{u}_d) - (1/\rho_l)\overrightarrow{\nabla} p$), internal viscous ($\mu_v$), surface tension ($a(T_d)$) and gravity ($m_d \overrightarrow{g}_z$) to modify their dynamics in the plasma chamber. The black bars represent the initial droplet count distribution in the size domain ($1\ \mu\text{m} \leq r_d \leq 8\ \mu\text{m}$) as shown in Fig 1 (a) at 0 msec. The atmospheric pressure plasma is non-thermal in nature in which the electrons have higher temperature than ions. Certainly, the gas mixture is heated by gaining energy from the discharge plasma. The droplets start absorbing heat energy from the gas mixture and then the strong evaporation of droplets is started during downward drag. The immediate surrounding temperature of the gas is reduced by a well-known impact of evaporation that further trickles down the rate of evaporation along the pulse of droplets. When the droplets become dispersed in APP, the increase in the rate of evaporation depends on the saturation condition of evaporation. This can be observed clearly by a decline in the counts as well as the size distribution of liquid droplets with the passage of time as shown in Fig. 1 (a). In this process, the small radii of droplets are evaporated rapidly, which can be confirmed

Copyright line will be provided by the publisher

with a comparison of red and blue bars in which the size domain ($0.7\ \mu$m $\leq r_d \leq 6.5\ \mu$m) at 5 msec is squeezed to ($0.1\ \mu$m $\leq r_d \leq 5.5\ \mu$m) at 10 msec.

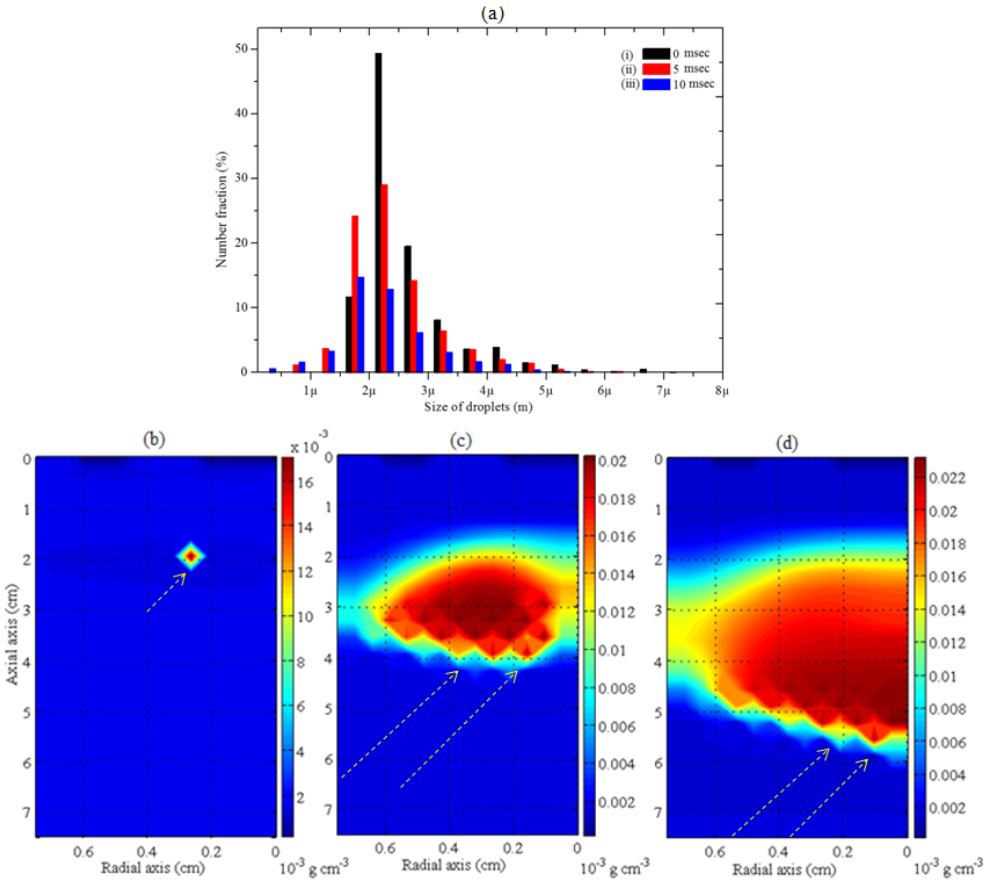

Fig. 1. Temporal profiles of (a) droplet counts and size distribution, and (b, c, d) spatial distribution of vapour species density using water droplets at precursor flow rate $= 50\ \mu$L min^{-1}, gas flow rate $= 5$ L min^{-1}, $f = 20$ kHz and $V_0 = -13.5$ kV in He-N_2 gas mixture.

Fig. 1 (b, c, d) indicates the evolution of the evaporation spreading during the downward flight of water droplets at the above-mentioned time instants (0 msec, 5 msec and 10 msec). When the droplets transform into vapours after obtaining enough energy from the gas mixture, they are recognized as another species in APP, termed as the vapour species density ($\rho_{gas}Y$). The constricted distribution as shown in Fig. 1 (b) represents the location of droplets' pulse injecting at 0 msec and it has a numerical value $\sim 0.165 \times 10^{-5}$ g cm^{-3}. With the passage of time, the density of vapour species amplifies due to evaporation of water droplets and its value enhances to $\sim 0.20 \times 10^{-4}$ g cm^{-3} at 5 msec in APP as shown in Fig. 1 (c). It is observed from the blue bars in Fig. 1 (a) that the size radii of droplets exist in the nanometer domain just before the phase shifting of liquid precursors. The continuous evaporation of droplets leads to an advancement in the vapour species density and it has a value of $\sim 0.23 \times 10^{-4}$ g cm^{-3} at 10 msec as shown in Fig. 1 (d). The increment in the vapour species density is primarily sharp from 0 msec to 5 msec, but it slows down notably from 5 msec to 10 msec because of the consistent enhancement of vaporization of droplets. This means that the advancement in evaporation is more rapid than the actual displacement of droplets in the chamber. In the course of the downfall of droplets, the gravitational as well as electrostatic forces exerted by the grounded substrate perform a major role to accelerate the dynamics of the droplets. From the above discussion, it is clear that the higher radii of droplets undergo a greater attractive gravitational pull than small radii of droplets. These spatio-temporal profiles provide a clear understanding in which the liquid phase is converted into vapour species density in the non-equilibrium APP. The droopy sharp points in the spatial distribution of vapour species density as shown with dotted arrows implies that they correspond to the droplets of various size distribution in the pulse of droplets at 5 msec and 10 msec.

Copyright line will be provided by the publisher

Consequently, the above discussion shows that the uniform properties of deposition can be accessed only as a consequence of the entire evaporation of droplets in the plasma chamber.

3.2 Temporal profiles of production rates

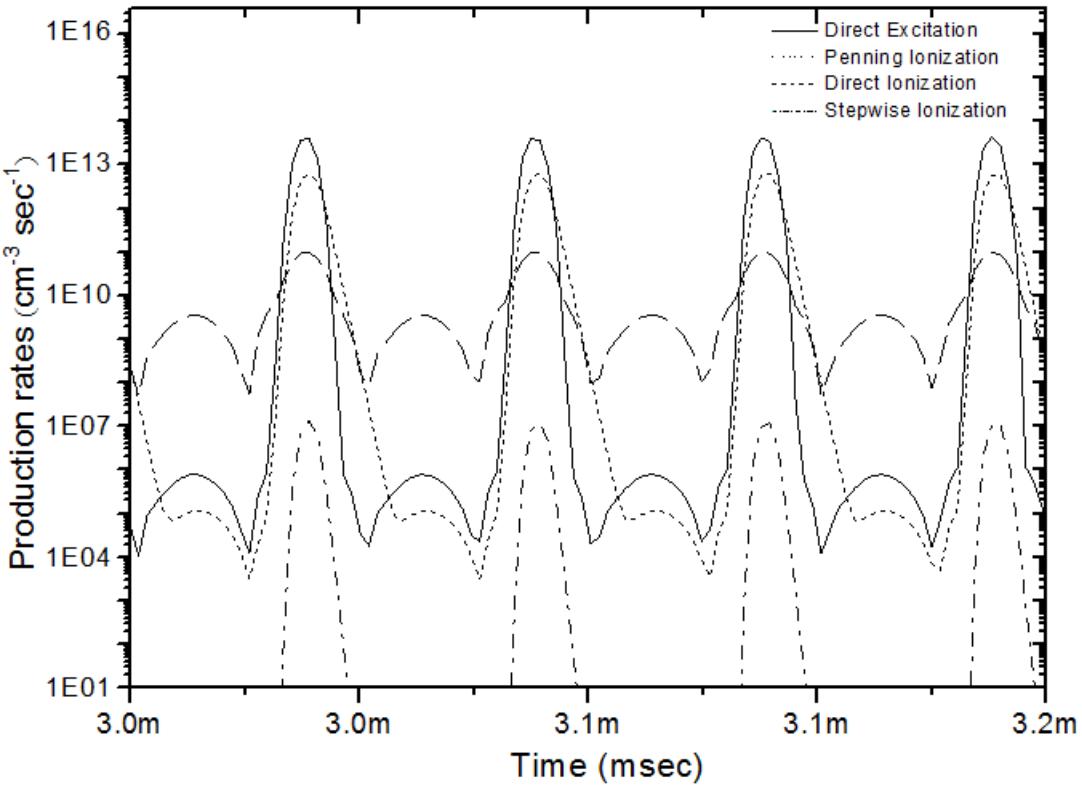

Fig. 2. Temporal evolution of line-averaged distribution of Direct excitation (DE), Penning ionization (PI), Direct ionization (DI) and Stepwise ionization (SI) rates using water droplets at precursor flow rate $= 50$ μL min^{-1} and gas flow rate $= 5$ L min^{-1}, $f = 20$ kHz and $V_0 = -13.5$ kV

To investigate the impact of chemical reactions during droplet-plasma interaction, the temporal profiles of line-averaged production rates of discharge species are considered to examine this complex phenomenon. In He-N_2 gas mixture, the nitrogen molecules have smaller ionization potential than the excitation potential of helium atoms; however, they can interact with metastables through Penning process. We consider a similar set of chemical reactions in this investigation as described in [22]. Since the oscillating sinusoidal potential is imposed on the thin metal electrode, the peaks of molecular helium and nitrogen ions are obtained near the metal electrode and grounded substrate at the maximum values of discharge current density during the alternate cycles of discharge current pulse. Due to strong peaks near the cathode and anode electrodes, the mean ionization rates of the entire chamber cannot provide a satisfactory explanation because of the strong production rates of electrons, ions and metastables near the electrodes. Hence in order to describe the production rates of charged particles along the pulse of droplets, we are averaging the rectangular area of chamber to analyze the behavior of interaction by ignoring the areas near the cathode and grounded substrates. In this way, the main contribution of excitation and ionization activities can be explored along the pulse of liquid precursors. The production rate of direct excitation is represented by a solid line, whereas the Penning ionization corresponds to dotted line as shown in Fig. 2. The remaining direct and stepwise ionization mechanisms are shown with dashed and dash-dotted line.

Fig. 2 represents the temporal line-averaged distribution of different production rates enduring in the bulk of discharge plasma while indicating that the production rates of direct excitation and Penning ionization are more assertive than the direct and stepwise ionization mechanisms along the pulse of droplets. It is evident from the

Copyright line will be provided by the publisher

various ionization channels of production rates that the asymmetric temporal profiles are obtained for several consecutive cycles. The asymmetrical pattern of production rates shows that it develops due to the presence of asymmetric electrode geometry of PlasmaStream system. The rate of stepwise ionization has emerged as least effective because of the frequent mechanism of annihilation of metastables through the avenue of Penning ionization. This performs a decisive role to maintain the stability of atmospheric pressure plasma in the presence of trace amount of nitrogen impurities; otherwise, the APP will be transformed into a non-uniform mode. Due to substantial impact of PI process, the molecular nitrogen ions are prevalent along the pulse of droplets as compared to the atomic and molecular helium ions from DI as shown in Fig 2. The atomic helium ions from DI are immediately transferred to molecular helium ions through the channel of three body chemical reaction ($He^+ + 2He \rightarrow He_2^+ + He$) that are further converted into molecular helium ions by using the path of charge transfer mechanism. This transformation occurs due to the small life time of He^+ ions in the atmospheric pressure plasma. The molecular nitrogen ions strongly interact with liquid precursors along the pulse of droplets in the plasma chamber while the molecular helium ions are dominant near the surface of the momentary cathode electrode during the alternate cycles of external imposed oscillating potential. In APP, the metastables are vigorously interactive along the pulse of droplets acting as the principal source of ionization through Penning ionization process in the He-N_2 gas mixture. Thus the metastables do a pivotal role to control the desired characteristics of atmospheric pressure plasma in two-phase flow.

3.3 Significance of mutual interactions between droplets

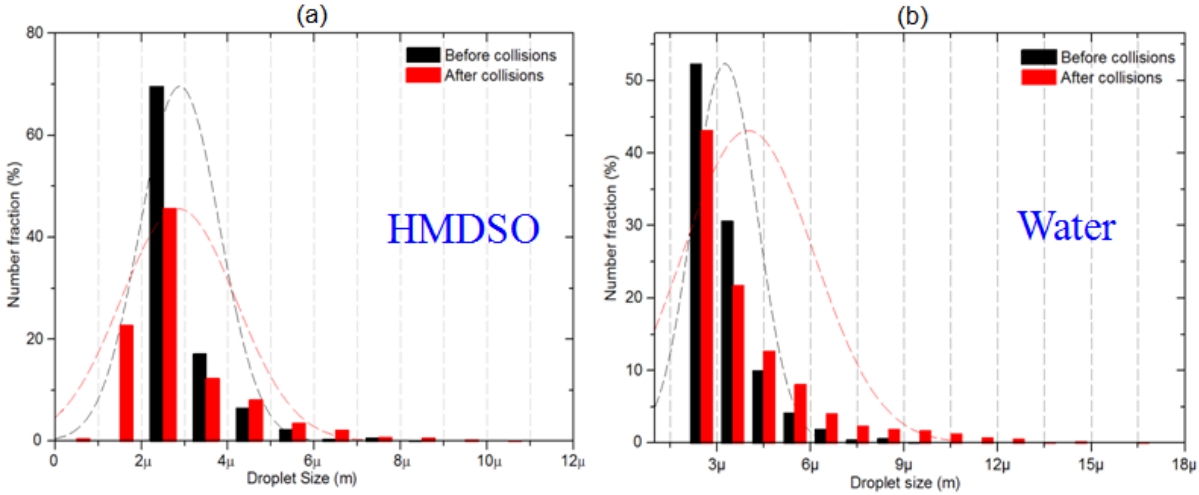

Fig. 3. Size distribution of the droplets before collisions (black bars at 0 msec) and after collisions (red bars at 1 msec) for (a) HMDSO and (b) water at precursor flow rate $= 100$ μL min^{-1} and gas flow rate $= 5$ L min^{-1}, $f = 20$ kHz and $V_0 = -13.5$ kV in He-N_2 gas mixture.

To analyze the major contribution of mutual interactions between liquid droplets in atmospheric pressure plasma, we consider two specific liquid precursors (HMDSO and water) because of their distinct nature under similar input driving conditions. It is observed from the numerical simulation results that the mutual interactions between the droplets are modified under the impact of different initial droplet injection velocities. This implies that the collisions are phenomenal just after injection of droplets' pulse in APP, which gradually becomes limited as they spread in the plasma chamber. Fig. 3 (a, b) provides the size radius and count distribution of HMDSO and water droplets before and after collisions. The coalescence and grazing of droplets are detected by using a similar principle as described in [23]. In case of coalescence of droplets, the radius of droplets increases, but the number of counts will fall. The position and velocity of droplets are adjusted during the grazing as well as coalescence of droplets. The fluid-droplet model is tested under different precursor flow rates, but it is noticed that the mutual interactions between the droplets are crucial at higher precursor flow rates (> 50 μL min^{-1}) rather than small flow rates. There are a small number of chances during the coalescence of droplets that the droplets acquire radii

Copyright line will be provided by the publisher

in the range (> 10 μm). The radii of droplets in the mentioned range are not evaporated in the plasma within the residence time of gas and their contribution divides into two parts. They partially evaporate in APP, while the remaining droplets with smaller radii are smashed on the substrate surface. Certainly, this is diagnosed as a major source of non-uniformity for the deposition of coatings. This reveals that the uniform deposition coating on the substrate can be possible only if the droplets of any radii must evaporate entirely within residence time

Fig. 3 shows the evaporation of droplets that is recognized as the prevalent mechanism in the case of HMDSO precursor droplets as compared to water droplets. This means that HMDSO is volatile in nature and it evaporates rapidly because of small surface tension than the water droplets as shown in Table 3. The water droplets have a greater mass density than HMDSO droplets and ultimately, they experience an intense gravitational pull during downward drag. Due to strong vaporization of HMDSO droplets, the smallest radii of droplets survive in the range (< 0.5 μm) just before the phase transformation as contrasted with red bars in Fig. 3 (a), whereas it is significantly higher for the water droplets as shown with red bars in Fig. 3 (b). Despite the slow evaporation of water droplets in discharge plasma, the coalescence events are momentous to provide their existence in the droplet size distribution. The size radii of water droplets are amplified after coalescing of droplets and its value shifts in the domain (2.0 μm $\leq r_d \leq 18$ μm). The dynamic viscosity of water is approximately double than HMDSO because of greater adhesiveness of water molecules, hence showing a higher probability of survival in the case of water droplets in the plasma chamber. Therefore, there is a greater tendency of cracking of water droplets on the substrate surface. These contrasting aspects and features signify a clear perspective that the evaporation is more aggressive for HMDSO droplets than water, which can be verified by the droplet count and size distributions as represented in Fig. 3 (a, b) before and after collisions.

4 Behavior of Evaporation in APP and Gas Mixture

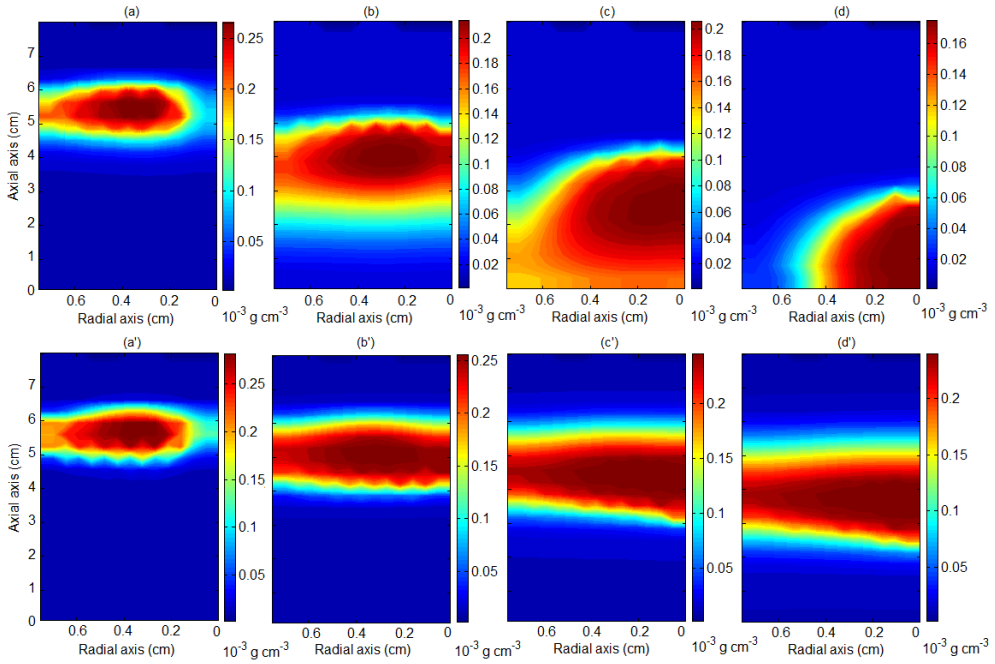

Fig. 4. Comparison of vapour species density in two different mediums, i) Atmospheric pressure plasma (top row), ii) He-N_2 gas mixture (bottom row) for HMDSO droplets at precursor flow rate $= 500$ μL min^{-1}, gas flow rate $= 5$ L min^{-1}, $f = 20$ kHz and $V_0 = -13.5$ kV.

In order to differentiate the behavior of droplets' interaction with two different mediums, such as discharge plasma and He-N_2 gas mixture, we inject a pulse of HMDSO liquid droplets into the plasma chamber spanning in the domain (4 μm $\leq r_d \leq 18$ μm) at 500 μL min^{-1}. A similar set of initial input parameters is considered in both cases to explore the reliability of numerical outcomes. The mutual interactions, named as grazing and coalescence

Copyright line will be provided by the publisher

of the droplets become critical at the mentioned precursor flow rate; however, the major interest lies here to distinguish the ramification of electrical forces on the droplets as mentioned in the set of Eqs. $(7-10)$. It has been discussed in [26] that the surface charge on the liquid droplet due to the floating potential is adequately less than the charge evaluated by the Rayleigh criterion. This prevents the droplets to break into small constituents. In both mediums, the droplets evaporate, but their rates of evaporation differ significantly. This section deals with the spatial distributions of vapour species density at four peculiar time instants, such as 5 msec, 10 msec, 15 msec and 20 msec to distinguish the impact of media on the droplets during traversing in the PlasmaStream system.

It is evident from the Fig. 4 that the evaporation of HMDSO droplets is identified as the commonly important during the initial 5 msec, but it changes extensively after this limit because of the strong heat gain of droplets in the discharge plasma. The evaporating pulse of droplets experiences a strong downward pull of electric potential that exerts force on the droplets while its magnitude depends on the radii of droplets as mentioned in Eq. (8). This means that the higher radii of droplets pass from the plasma chamber rapidly as compared to the He-N_2 gas mixture. The accomplished area of evaporation is greater in discharge plasma than the gas mixture, which is clearly contrasted from the top row in Fig. 4 (b - c) to bottom row in Fig. 4 (b′ - c′) of vapour species density. As a consequence, the smaller value of vapour species density is obtained in the case of APP than the gas mixture as shown in Fig. 4. In APP, the evaporation of droplets increases consistently; however, it turns into sluggish state in the medium of gas mixture. This occurs due to saturation of evaporation of droplets in the gas mixture. The downward pull of vapour species density is observed because of the presence of electrical force in He-N_2 discharge plasma, which attracts or repels HMDSO droplets towards the grounded substrate surface relying upon the polarity of a thin cathode electrode. The top row in Fig. 4 (a - d) shows that the pulse of droplets swiftly crosses the entire plasma channel than the gas mixture indicating the dominance of electric field that also reduces the residence time of HMDSO droplets. The duration of evaporation for the entire pulse of droplets becomes half in the case of APP than gas mixture. From the above discussion, it is obvious that the behavior of evaporation is diagnosed as a distinct mechanism in both mediums during two-phase flow. The bottom row in Fig. 4 (a′ - d′) provides a clear indication of surviving the pulse of droplets in the gas mixture without any downward pull as distinguished with APP.

5 Effect of Gas Flow Rates

Under the influence of distinctive gas flow rates, the spatial patterns of gas temperature and electron mean energy are discussed by applying same executing conditions. The droplets acquire a stationary state during downward fall, which indicate that the initial velocity has significant impact only for the mutual interactions rather than after settling in the plasma chamber. The local mass flux ratio ($\rho_d u_d / \rho_{gas} u_{gas}$) varies during the transport of two-phase flow until the entire bunch of liquid droplets transform into the vapour phase. The gas temperature reduces in the vicinity of droplets' pulse by the contribution of evaporation process. The perturbation produced by the droplets in the gas mixture becomes progressively large with an increment of gas flow rate as shown in Fig. 5 (a - c). The interaction between the droplets and discharge plasma is modified by an increment of the gas flow rate, but it also depends on the chemistry of gas in two-phase flow that is capable of effecting on the vaporization of droplets. The gas absorbs heat energy from the discharge plasma and subsequently, it results as a productive advancement in the evaporation of droplets in APP. Consequently, the temperature of gas mixture curtails along the pulse of droplets from 5 L min^{-1} to 20 L min^{-1} and the length of evaporation is amplified by an increment of gas flow rate.

Copyright line will be provided by the publisher

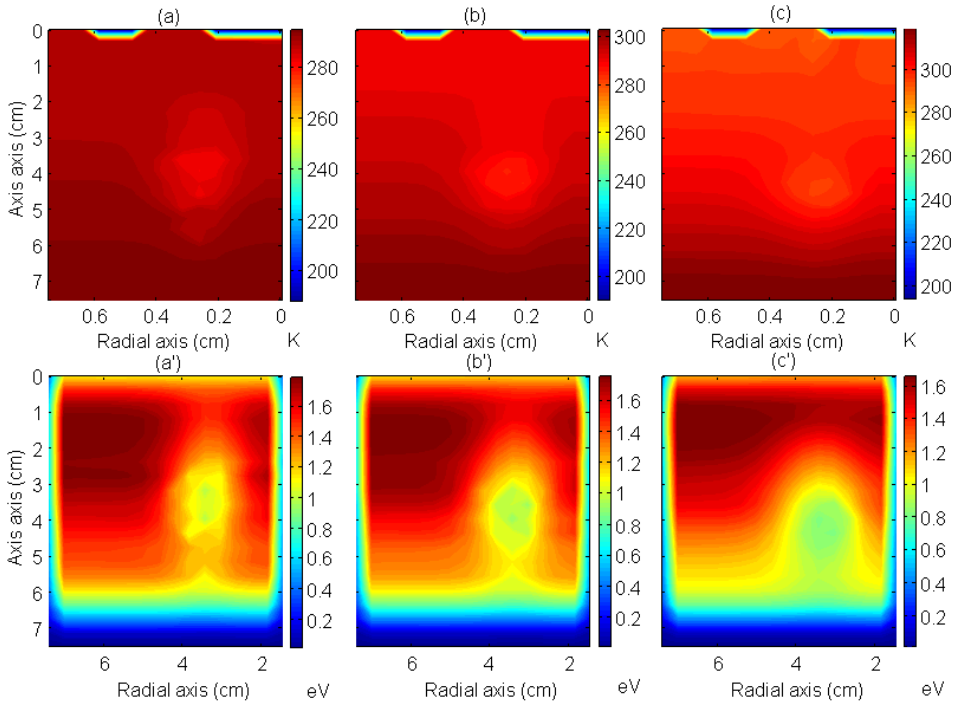

Fig. 5. Spatial distribution of (a, b, c) gas temperature and (a′, b′, c′) electron mean energy using HMDSO droplets at precursor flow rate $= 100\ \mu$L min^{-1}, gas flow rate $= 5, 10$ and 20 L min^{-1}, $f = 20$ kHz and $V_0 = -13.5$ kV in He-N_2 gas mixture.

Regarding the spatial distribution of electron mean energy, it is evaluated from the numerical solution of the electron energy density equation of the fluid model including the elastic and inelastic collision energy losses as well as joule heating as revealed in [22, 23]. The peak of electron mean energy is obtained near the thin cathode electrode and grounded substrate at the maximum values of discharge current density during the alternate cycles of discharge current pulse, despite the core interest lies in this case is to understand the dynamic modification in the structure of electron mean energy along the pulse of droplets. For this, the areas near the cathode and grounded substrate are ignored to explore the implication of evaporation on the electrons in the bulk of APP. It is clear from the spatial distributions as shown in Fig. 5 (a′ – c′) that the mean energy of electrons is smaller around the evaporating pulse of HMDSO droplets. The spatial spread of electron mean energy is greater at 20 L min^{-1} as compared to 5 L min^{-1} and 10 L min^{-1} indicating the rapid transfer of cooling downwards in the plasma chamber at a higher gas flow rate. This shows that the distribution of discharge plasma is altered during the transport and evaporation of droplets. The above spatial patterns of gas temperature and electron mean energy demonstrate that the length of cooling enhances with an increment of gas flow rate from 5 L min^{-1} to 20 L min^{-1}.

6 Influence of Different Precursors in APP

We now introduce different liquid precursors, such as HMDSO, nHexane, TEOS and water into He-N_2 atmospheric pressure plasma to explore the importance of their interaction in two-phase flow. The temporal profiles of the mean radius of droplets and mean vapour species density are obtained during the entire lifetime of droplets in the plasma chamber. It is clear from the Fig. 6 (a) that the pulses of HMDSO and nHexane droplets are evaporated rapidly as compared to TEOS and water droplets. This occurs due to the presence of strong intermolecular forces between the molecules of TEOS and water than other precursors. Fig. 6 (a, b) clearly indicates that the black solid line is used for HMDSO and red dashed line for nHexane, while the blue dotted line corresponds to TEOS and dark cyan dash-dotted for the water droplets. The variation in the rate of evaporation of different liquid precursors evolves due to the influence of many factors.

Copyright line will be provided by the publisher

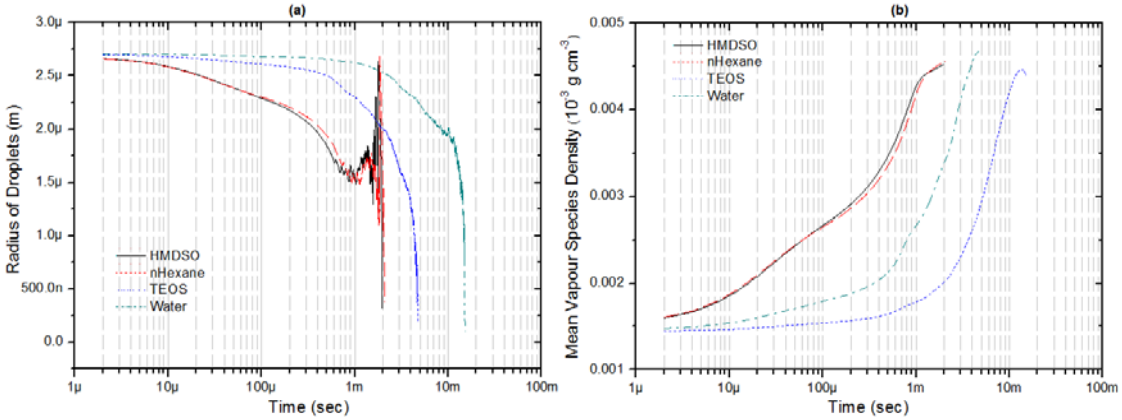

Fig. 6. Temporal mean distribution droplets' radii and vapour species density using HMDSO, nHexane, TEOS and water droplets at precursor flow rate $= 100$ μL min^{-1}, gas flow rate $= 5$ L min^{-1}, $f = 20$ kHz and $V_0 = -13.5$ kV in He-N_2 gas mixture.

It is clear from the temporal distribution of mean radius and vapour species density that the water droplets survives longer than other precursors as shown in Fig. 6. The increment in the vapour species density appears to be strong in the case of HMDSO and nHexane than other precursors, which occurs by the effect of the following factors, such as molecular weight, surface tension, dynamic viscosity as well as the existence of attractive forces between their molecules as illustrated in Table 3. If we compare the electronegative difference between the atoms of these precursors, it is noticed that H_2O has higher electronegative difference (1.4) than other precursors and hence the life time of water droplets is increased in the plasma chamber [27]. This suggests that the greater quantity of energy is required to annihilate the bonds between water molecules than other mentioned non-polar molecules. The London dispersion forces act as a glue for the binding of HMDSO, nHexane and TEOS molecules, which are typically weaker than hydrogen bonding of water molecules. The pulse of HMDSO droplet sustains for 1.10 msec whereas it is 11.1 msec for water in APP supporting the above arguments for the longer lifetime of water and TEOS precursors. Thus these results distinguish the role of interaction between various kinds of liquid precursors and APP in the PlasmaStream atmospheric pressure jet system.

The efficiency of the coupled fluid-droplet model can be checked by considering various liquid precursors under a similar set of operating parameters. This means that the properties of surface coating depend on the desolvation of precursors into the atmospheric pressure plasma. If the precursor droplets do not evaporate entirely within the residence time in APP, they ultimately break up after striking on the substrate surface. When a single droplet bursts on the substrate during plasma processing, the residues of droplet are sprinkled on the entire surface randomly. This acts as the starting point of developing a non-uniform deposition. These small residues of splashing droplet keep on growing with new incoming droplets. Hence in order to obtain a uniform deposition using precursor droplets in APP, the functioning conditions of gas and precursor flow rates are adjusted in such as way that the droplets must evaporate within the residence time and a specific time interval between the pulses should be present during injection to avoid the saturation of droplets' evaporation in discharge plasma. It is also observed from the outcomes of numerical modelling that the characteristics of APP rely on the initial distribution of droplets. The size radii of droplets should be present in the micron range (< 10 μm) for the complete evaporation in the discharge plasma, otherwise due to the effect of grazing and coalescence, the higher radii of droplets are formed and their eventual consequence is to splash on the substrate surface that causes a starting point of forming a non-uniform deposition.

Table 3. Numerical values of precursors used in Fluid-droplet model (FD2d) collected from [28]

Liquid Precursors	HMDSO ($C_6H_{18}OSi_2$)	nHexane (C_6H_{14})	TEOS ($C_8H_{20}O_4Si$)	Water (H_2O)
Surface Tension ($\times 10^3$ dyne cm^{-1})	1.57	1.84	2.28	7.28
Dynamic viscosity (dyne sec)	0.00488	0.0030	7.900	0.0089
Boiling point (K)	374.00	341.88	441.1	373.13
Mass Density ($\times 10^{-3}$ g cm^{-3})	764.00	660.00	934.0	1000.0

Copyright line will be provided by the publisher

7 Implication of Pure Helium and He-N_2 Gas Mixtures

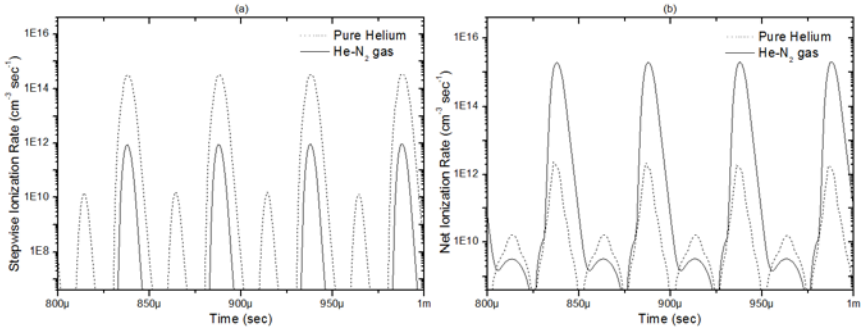

Fig. 7. Comparison of temporal profiles of line-averaged production rates of (a) Stepwise ionization and (b) Net ionization in the pure Helium and He-N_2 gas mixtures using HMDSO droplets at precursor flow rate $= 100$ μL min^{-1}, gas flow rate $= 10$ L min^{-1}, $f = 20$ kHz and $V_0 = -13.5$ kV.

Fig. 7 (a) shows the temporal profiles of line-averaged production rates of stepwise ionization in the pure helium and He-N_2 gas mixtures. In pure helium gas, the major sources of ionization are recognized as the direct and stepwise mechanisms, while the Penning ionization emerges as the appreciable in the case of He-N_2 gas mixture as compared to other production rates of ionization along the pulse of droplets. In this case, the stepwise ionization process identifies as the leading source of ionization in the pure helium gas as clearly shown by a dotted line and it occurs due to the existence of higher density of metastables. The numerical value of the rate of stepwise ionization is $\sim 2.0 \times 10^{14}$ cm^{-3} sec^{-1} in pure helium gas and it diminishes to $\sim 1.0 \times 10^{12}$ cm^{-3} sec^{-1} in He-N_2 gas mixture. Fig. 7 (b) provides the rate of net ionization in APP, which is combination of direct and Penning ionization mechanisms. The rate of annihilation of metastables is greater in the He-N_2 gas mixture occurring through Penning ionization. This wipes out the major quantity of metastables and ultimately, it enhances the rate of ionization in the bulk of APP. Subsequently, the density of metastables turns into a small quantity in the bulk of He-N_2 gas. It is evident from Fig. 7 (a, b) that the net ionization rate in He-N_2 discharge plasma is significantly larger than pure helium while its value $\sim 2.0 \times 10^{15}$ cm^{-3} sec^{-1} in He-N_2 slashes to $\sim 1.0 \times 10^{12}$ cm^{-3} sec^{-1} in pure helium gas. This disparity arises in the rate of net ionization because of the inclusion of Penning ionization process in the presence of trace amount of impurities as shown with a solid line in Fig. 7 (b). The vaporization of droplets boosts by the effect of net ionization in He-N_2 gas mixture and hence reduces the lifetime of droplets in the plasma chamber. Thus the above consequences provide a clear illustration that the rate of evaporation is amplified in the He-N_2 gas mixture as compared to pure helium gas, which is consistent with the previous simulation simulations [7].

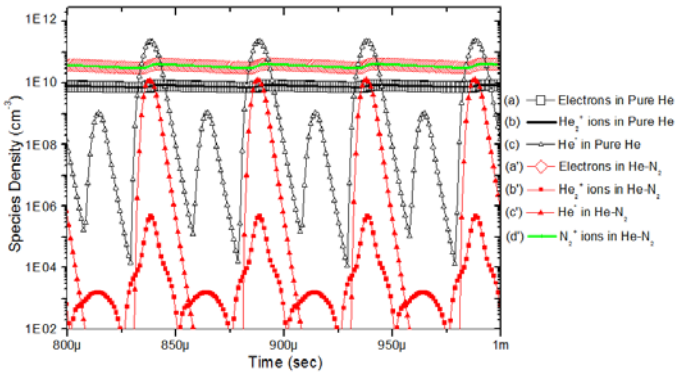

Fig. 8. Comparison of line-averaged species density (electrons, He_2^+ ions, N_2^+ ions and He^*) in the pure Helium and He-N_2 gas mixtures using HMDSO droplets at precursor flow rate $= 100$ μL min^{-1}, gas flow rate $= 10$ L min^{-1},$f = 20$ kHz and $V_0 = -13.5$ kV.

Copyright line will be provided by the publisher

Fig. 8 illustrates the line-averaged density distributions of discharge species, such as electrons, He_2^+ ions, N_2^+ ions and metastables (He^*) over various cycles in the pure helium using solid black lines plus symbols, while indicating with the red and green lines plus symbols in He-N_2 gas mixture. These temporal profiles are evaluated by ignoring the areas near the cathode and grounded substrate to explore the performance of droplet–plasma interaction during transport in the plasma chamber. The direct excitation is diagnosed as the central mechanism in the pure helium and He-N_2 gas mixtures, but the associated role of metastables becomes divergent in both gas mixtures. It is clearly observed from the line distribution of species density that the electrons and He_2^+ ions are responsible to maintain the quasi neutrality in the pure helium gas as shown in Fig. 8 (a, b). However, this situation is changed by the presence of nitrogen impurity molecules in He-N_2 gas, which results as the presence of the N_2^+ ions and electrons in APP as shown in Fig 8 (a′, d′). This clearly illustrates that the Penning process becomes the chief ionization mechanism of supplying the electrons along the pulse of droplets in He-N_2 discharge plasma. The line-averaged behavior of electrons shows that the ionization rate is enhanced by the evaporation of droplets because of the strong impact of Penning ionization as compared to direct and stepwise ionization rates. It is evident from the temporal distribution of metastables that they have greater density in the pure helium gas than He-N_2 gas mixture, which can be distinguished from the black line plus hallow triangle and red line plus solid triangles as shown in Fig. 8 (c, c′). This crop up by the destruction of metastables and its annihilation rate through Penning ionization exceeds in He-N_2 discharge plasma as compared to stepwise ionization in the pure helium gas mixture. As a result, the above discussion highlights that the prominent role of interaction between the droplets and plasma depends on the chemical reactions that are occurring during two-phase flow.

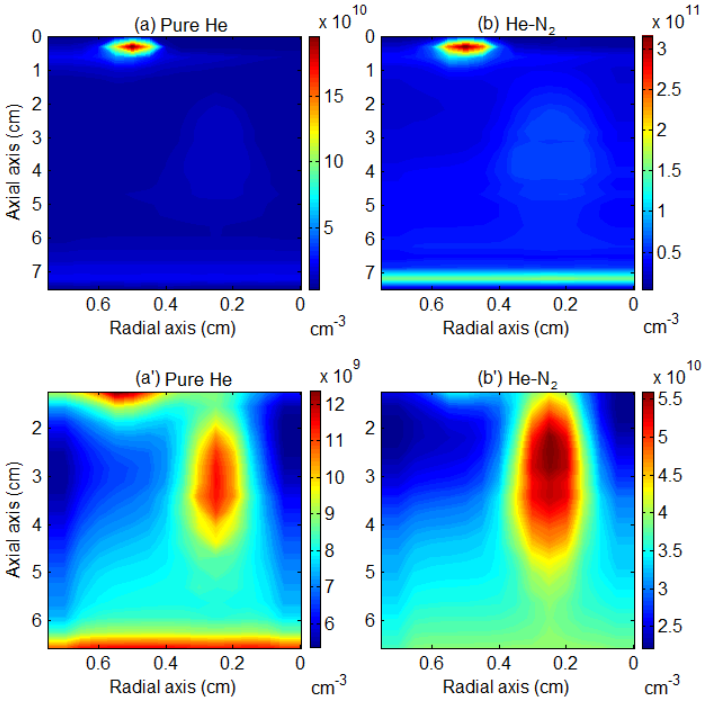

Fig. 9. Spatial distribution of (a, b) electron density in the plasma chamber, (a′, b′) electron density around the pulse of HMDSO droplets in the pure Helium and He-N_2 gas mixtures using HMDSO droplets at precursor flow rate $= 100$ μL min^{-1}, gas flow rate $= 10$ L min^{-1},$f = 20$ kHz and $V_0 = -13.5$ kV.

Fig. 9 manifests a clear contrast for the spatial distributions of electron density in the pure helium and He-N_2 gas mixtures under similar operating conditions. In both gas mixtures, the contour spatial distributions of electron density are obtained at the maximum value of discharge current density. The top row of electron density corresponds to the entire plasma chamber, while the bottom row represents the distribution along the pulse of HMDSO droplets ignoring the areas of thin cathode electrode and grounded substrate. This method provides a realistic understanding of electron dynamics along the pulse of evaporating droplets. The electron density is significantly greater near the thin cathode electrode than along the pulse of droplets in the case of pure helium gas, while its magnitude reduces from 1.91×10^{11} cm^{-3} to 1.22×10^{10} cm^{-3} as shown in Fig. 9 (a, a′). The

Copyright line will be provided by the publisher

similar trend in the contraction of electron density is observed in He-N_2 gas mixture in which the it changes from 3.15×10^{11} cm^{-3} to 5.55×10^{10} cm^{-3} as shown in Fig. 9 (b, b′). It is obvious from the transition in the magnitudes of the electron density that its value (2.595×10^{11} cm^{-3}) in He-N_2 mixture is greater than the value (1.788×10^{11} cm^{-3}) in the pure helium gas. The rate of evaporation is intensified by the strong impact of ionization in He-N_2 gas mixture that enhances further desolvation of droplets in APP. This creates a feasible environment in discharge plasma to achieve the desired uniform deposition coating.

Decomposition of HMDSO droplets is not present in the plasma chamber because of small precursor flow rates ($10-100$ μL min^{-1}). We have also checked the magnitude of surface charge on the droplets in the mentioned size domain of radii that is less than Rayleigh limit in atmospheric pressure plasma as discussed in [26]. It is observed from the spatial profiles of electron density that the area of ionization around the pulse of droplets is greater in He-N_2 gas, while it squeezes in pure helium gas mixture. This shows that the evaporation of droplets depends on the composition of operating gas mixture. If the gas mixture contains small amount of impurities that are capable of modifying the properties of discharge plasma and ultimately, the evaporation and mutual interactions of droplets are effected. In APP, the droplets act as the perturbing agent in the beginning; however, they become part of the operating gas mixture after phase transformation later as vapours. The entire set of interactions is glued through the coupling source terms, which provides a clear description of heat transfer in two-phase flow. The role of cold plasma can be manipulated by the control of precursor and gas flow rates because the rate of evaporation inflates with an increment of precursor and gas flow rates. This kind of cold APP is identified as suitable for the medical and industrial applications [$1-4$]. In case of incomplete evaporation of droplets, they are not considered as appropriate for the deposition applications due to presence of droplets in discharge plasma. From the above comparison, it is apparent that the nitrogen impurities are extremely helpful in strengthening ionization activities during carrier of gas in the plasma chamber, which further reinforces vaporization of droplets forming a uniform environment of plasma suitable for the surface coatings.

8 Three-dimensional Profiles of Atmospheric Pressure Plasma

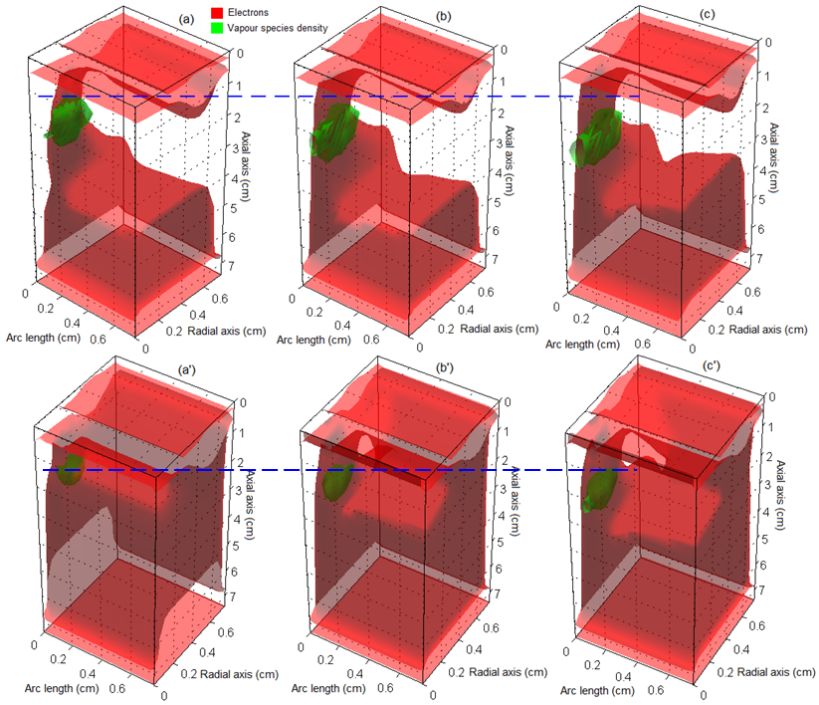

Fig. 10. Spatio-temporal iso-contours of electrons (red) and vapour species density (green) using TEOS (top row) and HMDSO (bottom row) at t_1, t_2 and t_3 msec at precursor flow rate $= 100$ μL min^{-1}, gas flow rate $= 5$ L min^{-1}, $f = 20$ kHz and $V_0 = -13.5$ kV.

Copyright line will be provided by the publisher

In this section, the three-dimensional profiles of atmospheric pressure plasma are considered to describe the dynamic aspects of evaporation using TEOS and HMDSO precursors under the same constraints. The reliability and authenticity of multi-dimensional (2D and 3D) numerical modelling outcomes have already been established in [23] by comparing with experimental measurements. Fig. 10 represents the iso-contours of electrons (red) and vapour species density (green) at three consecutive time instants ($t_1 = 0.6$ msec, $t_2 = 1.6$ msec and $t_3 = 2.6$ msec) during the evaporating pulse of TEOS and HMDSO precursor droplets in the plasma chamber. The iso-contours of vapour species density indicate that their volume expand with the passage of time in the case of both precursors, but the growth of volume due to evaporation of droplets is greater for TEOS than HMDSO in discharge plasma. This occurs by the existence of disparity in the mass density of TEOS and HMDSO droplets and hence the bunch of TEOS droplets experiences a larger gravitational pull than HMDSO and ultimately, it evolves as a difference in their volumetric spread as clearly contrasted in the top and bottom rows of Fig. 10. The effected volume along the pulse of droplets widens and drags downwards as illustrated with blue dashed line. On the other hand, the rate of vaporization of HMDSO droplets is greater than TEOS in He-N_2 discharge plasma because of its less surface tension and boiling point as compared to TEOS. This can be confirmed from Table 4 that shows greater values of vapour species density for HMDSO than TEOS, while these features are in accordance with the previous results discussed in section 6 using two-dimensional coupled fluid-droplet model.

At t_1, the conducting channel is in the process of building an intense ionization along the pulse of both precursor droplets, which can be distinguished as shown in Fig. 10 (a, a′). The overlapped density layers of electrons (red) and vapour species density (blue) are expanding as demonstrated in Fig. 10 (b, b′) at t_2 and the growth of vapour species will continue until the entire pulse of droplets dissolve in the discharge plasma. Regarding the kinetics of electrons, they are present in the entire plasma chamber at the maximum value of negative discharge current density as exhibited with red iso-contours in Fig. 10. This shows that the density of electrons increases progressively. The electron density is higher along the pulse of HMDSO droplets than TEOS, which can be verified from the numerical values mentioned in Table 4. The effected volume of vapour species is smaller in the case of HMDSO than TEOS because of the robust rate of evaporation in APP. In addition, it is observed from the numerical simulations that the duration of evaporation for the entire pulse of TEOS is approximately double than HMDSO droplets. This means that the scattering of droplets is higher in the case of TEOS than HMDSO droplets and as a consequence, the volume of vapour species becomes larger using TEOS. These observations can be clearly distinguished from the top and bottom rows as shown in Fig. 10. From the above discussion, it is obvious that the interactive behavior of liquid droplets with discharge plasma is dependent on the kind of precursor. Thus the numerical modelling results are perceived as satisfactory to provide decent understanding of droplet-plasma interaction in APP. These semi transparent volumetric profiles exhibit that the internal details of discharge plasma are quite complex in two-phase flow, which will be explained in more detail in the future simulation study by taking a complex chemistry set involving the chemical reactions between vapours and discharge species.

Table 4. Density of electrons and vapour species using three-dimensional Fluid-droplet model (FD3d)

Time/Density	$t_1 = 0.6$ msec	$t_2 = 1.6$ msec	$t_3 = 2.6$ msec	Precursor
Electron density (cm^{-3})	1.05×10^{11}	1.25×10^{11}	1.50×10^{11}	TEOS
Electron density (cm^{-3})	4.10×10^{11}	4.20×10^{11}	4.12×10^{11}	HMDSO
Vapour species density (g cm^{-3})	4.10×10^{-5}	4.70×10^{-5}	5.30×10^{-5}	TEOS
Vapour species density (g cm^{-3})	1.15×10^{-4}	1.25×10^{-4}	1.13×10^{-4}	HMDSO

9 Conclusions

In this simulation study, we have used multi-dimensional fluid-droplet model to explore the dynamics of liquid precursor droplets in APP by applying a distinct set of operating conditions. The mutual interactions, such as grazing and coalescence between the water droplets are identified as strongly assertive as compared to HMDSO at 100 μL min^{-1}, while the vaporization of HMDSO precursor becomes stronger than water droplets. The influence of evaporation of HMDSO droplets is contrasted in two different mediums that provide a clear indication of robust rate of evaporation of droplets in APP than gas mixture. The length of evaporation is enlarged by an increment of gas flow rate, which is confirmed with a gas temperature and electron mean energy demonstrating a displacement of local cooling in the plasma chamber. Penning ionization performs a leading role to enhance the

Copyright line will be provided by the publisher

rate of evaporation in He-N_2 discharge plasma, but the stepwise ionization process takes over other ionization mechanisms along the pulse of droplets in the pure helium discharge plasma. It is observed from the density distributions of discharge species that the metastables are responsible to maintain the ionization activities around the pulse of droplets in the pure helium and He-N_2 gas mixtures. Finally, the three-dimensional profiles of electrons and vapour species density are distinguished at three distinct time instants using TEOS and HMDSO precursors.

Table 1. List of variables along with description used in Eqs. $(1-11)$

Symbols	**Description**
ρ_{gas}	Mass density of gas
$\overrightarrow{u}$	Velocity of gas (u_r, u_z)
P	Pressure
$\overrightarrow{\Gamma}_{\mu}$	Momentum
k	Thermal conductivity
$\overrightarrow{j}$	Joule heating
$\overrightarrow{E}$	Electric field along radial (E_r) and axial direction (E_z)
h	Enthalpy
D_{AB}	diffusion coefficient
Y	vapour species mass fraction
C_p	Specific heat at constant pressure
$\overrightarrow{x}_p$	Position of droplets in the parcels
$\overrightarrow{u}_p$	Velocity of droplets in the parcels
r_p	Radius of droplets in the parcels
T_p	Temperature of droplets in the parcels
q_p	Charge on droplets in the parcels
m_p	Mass of droplets in the parcels
$\overrightarrow{u}'$	Velocity of gas with fluctuations
ρ_l	Density of liquid precursors
k_p	Boltzmann constant
g_z	Gravitational constant
R	Universal gas constant
$K_p = \frac{3}{8}\frac{\rho_{gas}}{\rho_l}\left(\left\|\overrightarrow{u}+\overrightarrow{u}'-\overrightarrow{u}_d\right\|/r_d\right)c_D$	Represents the evaluation of a variable
$c_D = (24/R_e)\left(1+R_e^{2/3}/6\right)$	c_D is used in the calculation of drag coefficient
$R_e = \left(2\rho_g\left\|\overrightarrow{u}+\overrightarrow{u}'-\overrightarrow{u}_d\right\|r_d\right)/\mu_{gas}(\overline{T}_{gas})$	Reynolds number
$\overrightarrow{F} = \begin{pmatrix} K_p\left(\overrightarrow{u}+\overrightarrow{u}'-\overrightarrow{u}_d\right) \\ -(1/\rho_l)\overrightarrow{\nabla}p + mg_z\widehat{k} + \lvert q_d\rvert\overrightarrow{E} \end{pmatrix}$	Forces acting on the droplets
n_e	Electronic flux around the droplet
q_e	charge on electrons
n_i	Ionic flux around the droplet
v_i	Average velocity of ions
$\overline{v}_e$	Average velocity of electrons
λ_{gas}	Heat conductivity of gas
$c_{p_{gas}}$	Gas specific heat at constant pressure
$\mu_{gas}(\overline{T}_{gas})$	Viscosity of gas
$\overline{T}_{gas} = \frac{(T_{gas}+2T_d)}{3}$	$\overline{T}_{gas}$ and T_{gas} are the average and local gas temperatures
$Nu_{(gas,l)}$	Nusselt number of gas and liquid
Y_{V_s}	Liquid vapour mass fraction on the surface of the droplet
Y_V	Liquid vapour mass fraction
$\mathrm{Pr} = \mu_{gas}c_{p_{gas}}/\lambda_{gas}$	Gas-phase Prandtl number

Copyright line will be provided by the publisher

Symbols	Description
c_l	Specific heat of liquid at constant pressure
T_s	Surface temperature of droplet
$P_{gas} = \rho_{gas} R T_{gas} \left(Y_V/W_V + Y_I/W_I\right)$	Equation of state
$h_l(T_d) = c_{p_V} T_d - L(T_d)$	Enthalpy of liquid droplets
$h_{gas} = \left(c_{pv} Y_V + c_{pI} Y_I\right) T_{gas} = c_{p_{gas}} T_{gas}$	Equation of state
W_V, W_I	Molecular weight of liquid vapours and gas
c_{pV}	Specific heat of vapour species at constant pressure
c_{p_I}	Specific heat of inert gas species at constant pressure
W_e	Weber number
$f^{'}(r_d) = (1/\overline{r}_d)\exp(-r_d/\overline{r}_d)$	X-squared distribution function
n_{sp}, μ_{sp}, T_{sp} and q_{sp}	Species density, mobility, temperature and charge
$S = -\int 4\pi r_d^2 \dot{r}_d \, \rho_d \, f^{'} \, d\overrightarrow{u}_d dr_d dT_d$	Source term for mass transfer
$\overrightarrow{S}_M = -\int f^{'} \rho_d \begin{pmatrix} \frac{4}{3}\pi r_d^3 \overrightarrow{F} \\ +4\pi r_d^2 \dot{r}_d \overrightarrow{u}_d \end{pmatrix} d\overrightarrow{u}_d dr_d dT_d$	Source term for axial momentum transfer
$S_E = -\int f^{'} \rho_d \begin{pmatrix} \frac{4}{3}\pi r_d^2 \dot{r}_d \, h_l(T_d) \\ +\frac{4}{3}\pi r_d^3 c_l \dot{T}_d \\ +\frac{4}{3}\pi r_d^3 \overrightarrow{F}.\overrightarrow{u}_d \\ -\frac{4}{3}\pi r_d^3 \overrightarrow{F}.\overrightarrow{u} \end{pmatrix} d\overrightarrow{u}_d dr_d dT_d$	Source term for gas enthalpy

Acknowledgements This work is supported by Science Foundation Ireland grant no. 08/SRC/I1411.

References

[1] Michael Thomas, K. L. Mittal, Atmospheric Pressure Plasma Treatment of Polymers: Relevance to Adhesion, John Wiley & Sons, Inc. Hobohen, New Jersey, ISBN 978-1-118-59621-0, (2013).
[2] M. Laroussi, IEEE Trans. Plasma Sci., **30**, No. 4, pp. 1409-1415, (2002).
[3] V. Nelea, Li Luo, C. N. Demers, J. Antoniou, A. Petit, S. Lerouge, M. R. Wertheimer and F. Mwale, J. Biomedical Materials Research, Part A, Vol. **75A**, Issue 1, pp. 216 – 223, (2005).
[4] G. Fridman, M. Peddinghaus, H. Ayan, A. Fridman, M. Balasubramanian, A. Gutsol, A. Brooks, G. Friedman, Plasma Chem. Plasma Process, pp. 425 – 442, **26**, (2006).
[5] M. Pasandideh-Fard, R. Bhola, S. Chandra, J. Mostaghimi, Int. J. Heat Mass Transf., p. 2229, **41**, (1998).
[6] Sameer A. Al-Bataineh, Endre J. Szili, Philipp J. Gruner, Craig Priest, Hans J. Griesser, Nicolas H. Voelcker, Robert D. Short, David A. Steele, Plasma Process. Polym., Issue 7, pp. 638 – 646, **9**, July (2012).
[7] C. P. Stallard, M. M. Iqbal, M. M. Turner and D. P. Dowling, Plasma Process. Polym., pp. 888 – 903, **10**, (2014).
[8] P. Zhang and U. Kortshagen, J. Phys. D: Appl. Phys., pp. 153 - 163, **39**, (2006).
[9] G. Este, W. D. Westwood, J. Vac. Sci. Technol., vol. **A2**, p. 1238, (1988).
[10] J. G. Birmingham, R. R. Moore, "Reactive Bed Plasma Air Purification," U.S. Patent no. 4, 954, 320, (1990).
[11] L. J. Gerenser, J. M. Grace, G. Apai, P. M. Thompon, Surf. Interf. Anal., pp. 12, **29**, (2000).
[12] K. H. Becker, U. Kogelschatz, and K. H. Schoenbach, Non-Equilibrium Air Plasmas at Atmospheric Pressure, Series in Plasma Physics, Taylor & Francis Group, ISBN 9780750309622 - CAT# IP501, (2004).
[13] P. J. O' Rourke, Collective Drop Effects in Vaporizing Liquid Sprays, Ph.D Thesis, 1532-T, Princeton University, (1981).
[14] P. Anthony, F. Herbert, L. O'Neill, J. Jaroszynska-Wolinska, C. Stallard, Amsarani Ramamoorthy, D. P. Dowling, Plasma Process. Polym., 230 – 238, **8**, (2011).
[15] Y. Shan and J. Mostaghimi, Spectrochimica Acta Part B **58**, p. 1959 – 1977, (2003).
[16] F. H. Harlow and A. A. Amsden, J. Computational Phys., 197 – 213, **8**, (1971).
[17] A. A. Amsden, P. J. O'Rourke, T.D. Butler, KIVA-II: A Computer Program for Chemically Reactive Flows with Sprays, Los Alamos National Laboratory report LA-11560-MS, May (1989).
[18] Z. Han, Li Fan and R. D. Reitz, SAE Transactions, 106 (**3**), 1423 – 1441, (1997).
[19] J. W. Olesik, L. J. Smith, E. J. Williamsen, Anal. Chem. , pp. 2002 – 2008, **61**, (1989).
[20] S. E. Hobbs and J. W. Olesik, Spectrochimica Acta. **40B**, No. 6/7, pp. 817 – 833, (1993).
[21] C. C. Leiby, JR. and H. J. Oskam, The physics of fluids, No. 9, **10**, September (1967).
[22] M. M. Iqbal, M. M. Turner, Contrib. Plasma Phys., No. 9, pp. 756 – 771, **54**, (2014).

Copyright line will be provided by the publisher

[23] M. M. Iqbal, C. P. Stallard, D. P. Dowling and M. M. Turner, Plasma Processes and Polys., ppap.201500003, 28 January (2015).
[24] M. A. Liberman, A. J. Lichtenberg, A John Wiley & Sons, Inc Publication, New Jersey, ISBN 0-471-72001-1, (2005).
[25] A. Fridman. Plasma Chemistry, Cambridge University Press, New York, ISBN-13 978-0-521-84735-3 hardback, (2008).
[26] M. M. Iqbal, M. M. Turner, Proceeding in 63rd Annual GEC and 7th ICRP, No. 7, **54**, Paris, France, October 4 - 8 (2010).
[27] H. Ralph, F. Petrucci, F. Geoffrey Herring, J. D. Madura, C. Bissonnette, General Chemistry: Principles and Modern Applications, Pearson/Prentice Hall, Upper Saddle River (2007).
[28] Wolfram|Alpha: Wolfram Alpha LLC, (2012).

Copyright line will be provided by the publisher